TECHNOLOGICAL UNIVERSITY DELFT

DEPARTMENT OF AERONAUTICAL ENGINEERING

Report VTH-124

THEORETICAL AND EXPERIMENTAL INVESTIGATIONS OF INCOMPRESSIBLE LAMINAR BOUNDARY LAYERS WITH AND WITHOUT SUCTION

Ph.D THESIS

J.L. van INGEN

DELFT
the NETHERLANDS

OCTOBER, 1965

This PDF-file contains chapter 10:

Experimental investigation of the laminar boundary layer on an impervious 28% thick airfoil section

.0. Experimental investigation of the laminar boundary layer on an impervious 28°/o thick airfoil section.

.0.1. Introductory remarks.

In section 8.13 the experiments of Schubauer on the laminar boundary layer of an elliptic cylinder have been discussed. It was mentioned that some controversy exists about these measurements since it was definitely shown in the experimental investigation that separation of the laminar boundary layer occurred while some boundary layer calculation methods fail to predict separation using the measured pressure distribution.
It was shown by Hartree that a slight modification of the measured pressure distribution is sufficient to obtain separation. However, it is not known for certain whether or not the change assumed by Hartree remains within experimental error.
Due to the uncertainty about the exact pressure distribution to be used, this experiment failed to definitely answer the question whether boundary layer theory is capable of predicting laminar separation using the measured pressure distribution.
Therefore it was thought worth while to undertake an independent investigation to provide additional - and possibly still more accurate - material to be used for a comparison between boundary layer theory and experiment.
A disadvantage of Schubauer's investigation is the small size of the model (11.78 inch chord) and the low speed (11.5 ft/sec) at which the measurements were performed, resulting in the low value of 72000 for the Reynoldsnumber R_c based on chord. Due to this low Reynolds number a fully separated laminar boundary layer occurred without subsequent turbulent reattachment.
Since the Reynoldsnumbers in aeronautical practice are much higher than 72000 it was thought worth while to perform the new investigation at a much larger value of R_c. The measurements were made on the upper surface of a 28°/o thick symmetrical airfoil section with a chord length of 1 meter. All measurements were made at zero angle of attack and a wind speed of 28 m/sec corresponding to $R_c = 1.37 \times 10^6$. This value of R_c was selected to ensure that a separated laminar boundary layer occurred

with subsequent turbulent reattachment.
Details of the test set-up and the apparatus used are mentioned in section 10.2; the test methods are described in section 10.3. Results of the measurements and a comparison with boundary layer theory are given in sections 10.4 and 10.5 respectively.

10.2. Description of the experimental apparatus.

10.2.1. The wind tunnel.

The experiments were performed in the low speed wind tunnel of the Department for Aeronautical Engineering at Delft Technological University. The test section of the wind tunnel has an octagonal cross section, 1.80 m wide and 1.25 m high; the maximum windspeed is 120 m/sec. At the speed employed for the present investigation (28 m/sec) the degree of turbulence is about 0.04°/o. Further details of this wind tunnel may be found in [108] and [109].

10.2.2. The model.

The wing model was not built for the present investigation but happened to be available. It had earlier been used by the N.L.L. at Amsterdam for some drag measurements.
The model is built up from two wooden spars and a number of wooden ribs spaced 140 mm apart. Furthermore the 2 mm thick multiplex skin is, at 135 mm intervals, supported by spanwise stringers.
The airfoil section used is NACA0028-64; the dimensions of which are given in table 10.1.
The model was placed vertically between the floor and ceiling of the test section; the geometric span obtained in this way being 1.25 m. A sketch, showing the test set-up is given as fig. 10.1.
Two rows of pressure orifices were provided in the upper surface of the model extending for some distance around the leading-edge to the lower surface. Positions of the orifices are given in table 10.2; those numbered 1-34 have been present during the whole series of measurements; the numbers 35 to 41 were added later during the investigation.

10.2.3. Hot-wire equipment.

Mean velocity profiles of the laminar boundary layer were measured with hot-wires at different positions in chord number III (fig. 10.1). Platinum wires, 0.003 mm Ø and about 2.5 mm long were used together with some transistorized equipment operating in the constant temperature mode. This equipment has been described in detail in [110].
The probe holding the hot-wire could be traversed across the boundary layer by means of a screw spindle (pitch 1 mm) running through a streamlined tube and extending through a hole in the sidewall of the wind tunnel. A dial at the end of the spindle enabled the displacement of the hot-wire, from an arbitrary reference position outside the boundary layer, to be read within 0.01 mm. The distance between this reference position and the model surface was determined by a special technique to be described in section 10.3.3.

10.2.4. Other apparatus.

The free stream speed U_∞ in the test section was measured by means of a pitot-static tube mounted some distance above the floor of the test section (fig. 10.1).
For all pressure measurements inclined tube manometers were used, frequently calibrated against a Betz-type manometer.
Besides the orifices in the model surface a small static tube - which could be taped to the surface - was used for the pressure distribution measurements. Total pressures inside the boundary layer at a fixed small distance from the wall were measured with a small flattened total head tube which could also be taped to the surface. Both tubes were soldered to a common base plate to form one instrument as shown in fig. 10.2.

10.3. Test methods and reduction of data.

10.3.1. Pressure distribution measurements.

At a free stream speed U_∞ = 28 m/sec the pressure distribution around the model was measured relative to the free stream total head p_t. Since

for subsequent boundary layer calculations the velocity U at the edge of the boundary layer is needed, the measured surface pressures p_x were converted to U. Using the assumption that the difference in static pressure between the wall and the edge of the boundary layer can be neglected, U follows from

$$\tfrac{1}{2}\rho U^2 = p_t - p_x \qquad (10.1)$$

The values of U obtained in this way were made non-dimensional with the free stream velocity U_∞.

It was found that inserting the hot-wire probe and the streamlined tube had some influence on the pressure distribution. Therefore some measurements were repeated with the hot-wire placed at two different chordwise positions in the lower chord with orifices.

Since the size of the model is rather large compared with the dimensions of the test section there must be an appreciable tunnel wall effect on the pressure distribution. Moreover the speed at the position of the pitot-static tube can not be regarded as true free stream speed since it will be influenced by the presence of the model and the walls. These effects present no real problem since it is the only object of the present investigation to compare boundary layer theory and experiment for the same - but otherwise arbitrary - pressure distribution. The "free-stream speed" U_∞ is only used as a reference speed to obtain non dimensional quantities.

It is clear however, that the present investigation will not predict the free-flight characteristics of the airfoil section.

10.3.2. Hot-wire measurements.

All hot-wire measurements were made in the mid-span chord. During these measurements frequent calibrations were obtained using the following procedure. The hot-wire was placed in the midspan position well outside the boundary layer at the same chordwise position as orifice number 23. Assuming two-dimensional flow and constant static pressure across the boundary layer the speed U at the position of the hot-wire follows from $\tfrac{1}{2}\rho U^2 = p_t - p_{23}$, where p_{23} is the static pressure at the position of

orifice number 23 and p_t is the free stream total head. By varying the tunnel speed and recording both $\frac{1}{2}\rho U^2$ and the output of the hot-wire apparatus a calibration curve is easily obtained.

Once the calibration is known a velocity profile can be measured by moving the hot-wire in small steps from well outside the boundary layer to about 0.10 mm from the model surface. There is no point in measuring closer to the wall since the corrections to be applied to hot-wire readings obtained near a wall are uncertain. Fortunately it is not necessary to perform measurements near the wall since the velocity profile in this region can easily be calculated as soon as the pressure distribution is known (see section 10.3.3.).

Although the displacement of the hot-wire can accurately be measured with reference to an arbitrary starting position, its absolute distance from the wall can not so easily be determined directly. It was found however that the compatibility conditions of the boundary layer equations provide an easy method to find this distance. This procedure will be described in the next sub-section.

10.3.3. Determination of the position of the hot-wire relative to the wall.

From the hot-wire measurements and the subsequent data reduction the non-dimensional velocity $\bar{u} = u/U$ in the boundary layer is found as function of the distance y_r measured from an arbitrary reference position outside the boundary layer (fig. 10.3). A problem remaining to be solved is to determine the distance between this reference position and the wall. This was done as follows using the compatibility conditions (2.10) and (2.11).

$$v_o\left(\frac{\partial u}{\partial y}\right)_o = U\frac{dU}{dx} + \nu\left(\frac{\partial^2 u}{\partial y^2}\right)_o \qquad (10.2)$$

$$v_o\left(\frac{\partial^2 u}{\partial y^2}\right)_o = \nu\left(\frac{\partial^3 u}{\partial y^3}\right)_o \qquad (10.3)$$

Equations (10.2) and (10.3) show that $\left(\frac{\partial^2 u}{\partial y^2}\right)_o$ and $\left(\frac{\partial^3 u}{\partial y^3}\right)_o$ can be calculated when v_o, $U\frac{dU}{dx}$ and $\left(\frac{\partial u}{\partial y}\right)_o$ are known. This implies that in the

Taylor series expansion of the velocity near the wall

$$u = \left(\frac{\partial u}{\partial y}\right)_o \frac{y}{1!} + \left(\frac{\partial^2 u}{\partial y^2}\right)_o \frac{y^2}{2!} + \left(\frac{\partial^3 u}{\partial y^3}\right)_o \frac{y^3}{3!} + \ldots\ldots \qquad (10.4)$$

the coefficients of y^2 and y^3 are known if - apart from the pressure- and suction distribution - the coefficient $\left(\frac{\partial u}{\partial y}\right)_o$ is given.

The procedure adopted now is to calculate the velocity profile near the wall from equation (10.4) for some assumed values of $\left(\frac{\partial u}{\partial y}\right)_o$. These velocity profiles are then plotted on a sheet of transparant paper which is placed on the measured curve in such a way that one of the calculated profiles coincides with the measured profile over some distance near the wall. Using this procedure not only the position of the wall is found but also a value for the wall shear stress is obtained. It may be noted from equation 10.2 and 10.3 that for the present case of impervious walls ($v_o = 0$) the derivatives $\left(\frac{\partial^2 u}{\partial y^2}\right)_o$ and $\left(\frac{\partial^3 u}{\partial y^3}\right)_o$ follow directly from

$$\left(\frac{\partial^2 u}{\partial y^2}\right)_o = -\frac{U}{\nu}\frac{dU}{dx} \qquad (10.5)$$

$$\left(\frac{\partial^3 u}{\partial y^3}\right)_o = 0 \qquad (10.6)$$

10.3.4. Measurements with the surface tubes.

From the difference in pressure indicated by the flattened total head tube and the static tube, shown in fig. 10.2, the value of $\frac{1}{2}\rho u^2$ at a small distance from the wall is found. This device may then be used to obtain a rough estimate of the wall shear stress and the position of separation. It is not possible to get accurate values in this way due to the fact that the distance between the wall and the effective center of the total-head tube is not known.

10.3.5. Flow visualization experiments.

It was attempted to determine the separation point of the laminar

boundary layer by means of the oil film technique and using smoke. No sharp indication of separation could be obtained in this way. The position of reattachment of the turbulent boundary layer, however, was clearly indicated by the oil film.

10.4. Results of the experiments.

10.4.1. The pressure distribution.

Detailed results of the pressure measurements have been collected in table 10.3. Fig. 10.4 shows $\overline{U}$ as function of $\overline{x}$ for the lower chord with orifices without the boundary layer traversing gear present. Values of $\overline{U}$ obtained with the static tube are consistently about $0.5^{o}/o$ lower than those determined from the orifices. Therefore the results of the static tube have been used only as an aid to draw a proper curve through the points resulting from the orifices. The full curves drawn in fig. 10.4 give the relations between $\overline{U}$, $\frac{d\overline{U}}{d\overline{x}}$ and $\overline{x}$ which finally have been adopted for the boundary layer calculations (See also table 10.4). Near the leading-edge ($-0.04 < \overline{x} < +0.04$) the measurements may be approximated by

$$\overline{U} = 21.987\ \overline{x} - 2218.8\ \overline{x}^{3} + 221907\ \overline{x}^{5} \qquad (10.7)$$

In the interval $0.12 < \overline{x} < 0.18$ an irregularity in $\overline{U}(\overline{x})$ occurs; this region is shown to a larger scale in fig. 10.5. It is possible that the oscillation in $\frac{d\overline{U}}{d\overline{x}}$ is caused by inaccurate manufacturing of the model but it may equally well originate from the procedure by which the airfoil sections are designed. It is usual to compute the coordinates of a limited number of points of a section which in general is not sufficient to fix the shape in every detail. Especially in the region near the leading-edge, where rapid changes in curvature occur, the pressure distribution may be very sensitive to small deviations from the desired contour. Support to this idea is given by the fact that for the suction model, to be described in chapter 11, a similar irregularity occurred.

There is a sharp discontinuity in the pressure distribution near $\overline{x} = 0.71$; this is caused by transition of the separated laminar

boundary layer and subsequent turbulent reattachment. Separation occurs upstream of this point at about $\bar{x} = 0.64$ (see section 10.4.2).
The region from $\bar{x} = 0.40$ to 0.80 is shown to a larger scale in fig. 10.6. This figure reveals a second discontinuity in the slope of the curve near $\bar{x} = 0.635$. It will be shown in section 10.4.2. that this irregularity corresponds to the separation point of the laminar boundary layer.
Results for the upper row of orifices are very nearly the same as those for the lower row (see table 10.3); therefore in what follows it will be assumed that the pressure distribution is two-dimensional.
Inserting the boundary layer traversing gear in the wind tunnel lowers the values of $\bar{U}$ upstream of the hot-wire by about $0.5^{o}/o$. The shape of $\bar{U}(\bar{x})$ however remains essentially the same. The values of $\bar{U}$, with the traversing gear present, can be made equal to those without it by decreasing U_∞ by about $0.5^{o}/o$; this implies adopting a $0.5^{o}/o$ lower value of the Reynoldsnumber R_c. Remembering that the boundary layer parameters $\bar{\delta}^*$, $\bar{\Theta}$, H and the non-dimensional wall shear stress ℓ only depend on the function $\bar{U}(\bar{x})$, and not on the value of R_c, it is clear that changing R_c will have no influence on the position of separation.
The boundary layer thickness is inversely proportional to $(R_c)^{\frac{1}{2}}$ and hence the boundary layer thickness will increase $0.25^{o}/o$ due to the presence of the boundary layer traversing gear. It can not be expected that this difference will be noticed in the experiments.
Therefore in all subsequent analyses of the experimental results and boundary layer calculations the pressure distribution as determined for the lower chord, without the traversing gear present, has been used (table 10.4).
The values of $\bar{U}$ quoted in table 10.4 have been obtained from large scale versions of fig. 10.4 to 10.6; the derivatives $\frac{d\bar{U}}{d\bar{x}}$ have been found by numerical differentiation. It is emphasized at this point that slight changes in $\bar{U}(\bar{x})$ may produce large variations in $\frac{d\bar{U}}{d\bar{x}}$. There is scope for a different fairing of the experimental results, especially near the irregularity at $\bar{x} = 0.15$ and near separation. This may have an appreciable effect on the boundary layer calculations.

10.4.2. Results of the boundary layer measurements.

The measured velocity profiles are shown in fig. 10.7; the values of $\bar{u}$ as determined from equation 10.4 have been included to show how this equation fits the measurements. Some points measured very near the wall should be disregarded since these results may have been influenced by some disturbing factors. In the first place the calibration of the hot-wire is not valid when measuring very near a wall. In the second place the prongs holding the wire may have been in contact with the wall leading to an extra heat loss of the wire. Moreover - and this is probably the most important factor - the prongs may bend, leading to an erroneous value for y. Included in fig. 10.7 are the velocity profiles determined from the boundary layer calculations to be discussed in section 10.5. Fig. 10.8 shows a comparison between the experimentally determined and calculated values of $\bar{\delta}^*$, $\bar{\theta}$ and H. The wall shear stress, obtained from the procedure outlined in section 10.3.3, is shown in fig. 10.9 where the results of boundary layer calculations are also given. The measurements seem to indicate that zero skin friction, and hence separation, will occur near $\bar{x} = 0.64$.

Included in fig. 10.9 are the results of measurements with the combined total head- and static tubes. For comparison the values of $\bar{u}$ at constant distances from the wall, as obtained from a cross plot of fig. 10.7, have also been given. The results indicate that the effective distance of the total head tube from the wall is nearly constant at a value between 0.25 and 0.30 mm for $x < 0.44$. For $x > 0.45$ the effective distance in general increases in the downstream direction especially when separation is approached. The velocity indicated by the tube tends to zero for $\bar{x} \rightarrow 0.665$ implying that the tube enters the region with backflow for $\bar{x} > 0.655$.

It has been shown by Goldstein [84] (see also section 8.9) that near a separation point τ_o should behave like $(\bar{x} - \bar{x}_s)^{\frac{1}{2}}$ where $\bar{x}_s$ denotes the separation point. Therefore it is appropriate to plot τ_o^2 versus $\bar{x}$ near separation. This has been done in fig. 10.10; it is found indeed that a straight line can be drawn through the measured points. Extrapolating to zero shear stress indicates separation at $\bar{x} = 0.637$;

this is so close to the value $\bar{x} = 0.635$ where a discontinuity in $\frac{d\bar{U}}{d\bar{x}}$ occurs, that it may be assumed that the irregularity in $\bar{U}(\bar{x})$ is due to the presence of the separation bubble.
Also shown in fig. 10.10 is $\bar{u}_p^2$; where $\bar{u}_p$ is the value indicated by the total head- and static tube combination. It follows that $\bar{u}_p^2$ becomes zero at $\bar{x} = 0.655$; remains negative until $\bar{x} = 0.716$; rises very fast downstream of $\bar{x} = 0.716$ and levels off again at about $\bar{x} = 0.80$. It is noted that $\bar{u}_p^2$ is not to be interpreted as the square of a velocity when negative; since the total head tube will not indicate total head but nearly static pressure when placed in a reversed flow.
Combining the information obtained from all the measurements described above suggests the following description of the flow near separation (see also fig. 10.11). Separation of the laminar boundary layer occurs at $\bar{x} = 0.635 - 0.637$ causing a small kink in the $\bar{U}(\bar{x})$ curve. At $\bar{x} = 0.655$ the effective center of the total head tube passess through the upper boundary of the region with reversed flow. Near $\bar{x} = 0.71$ transition of the separated layer occurs resulting in a sudden decrease of the displacement thickness and consequently in a large discontinuity in the curve for $\bar{U}(\bar{x})$. Near $\bar{x} = 0.716$ reattachment of the turbulent layer sets in while at $\bar{x} = 0.80$ a fully attached turbulent boundary layer occurs.

10.4.3. Results of the flow visualisation experiments.

Oil film technique. Due to the low speed at which the experiments were performed the aerodynamic forces on the oil were very small especially near separation. On the other hand, since the model surface was vertical, there was a strong influence of gravity forces on the direction of the oil flow. Therefore no reliable indication of separation could be obtained; from various trials it was conjectured however that separation occurs at $\bar{x} = 0.65 \pm 0.01$. Turbulent reattachment was shown very clearly to start at $\bar{x} = 0.71$ while a fully reattached turbulent boundary layer flow appeared to occur downstream of $\bar{x} = 0.74$.

Smoke injection. As the results of the oil film experiments were not conclusive it was tried to find the separation point by introducing smoke into the downstream end of the separation bubble. A very thin layer with reversed flow became clearly visible due to forward movement of the smoke in the bubble. Due to its small thickness the forward edge of the bubble was difficult to estimate; it was certainly upstream of $\bar{x} = 0.66$ however.

10.5. Boundary layer calculations using the measured pressure distribution.

10.5.1. The momentum method.

The pressure distribution used for the boundary layer calculations has been defined by equation (10.7) for $0 \leqslant \bar{x} \leqslant 0.04$ and by table 10.4 for $0.04 \leqslant \bar{x} \leqslant 0.70$. From $\bar{x} = 0$ to 0.04 equation (5.40) was employed with $\bar{x}_1 = 0$, $a_1 = 0.415$ and $b_1 = 4.84$; a step by step solution starting from $\bar{x} = 0.01$ gave essentially the same results at $\bar{x} = 0.04$. At $\bar{x} = 0.04$ a step by step calculation was started using steps of 0.01; from $\bar{x} = 0.12$ to 0.18 and 0.46 to 0.51 also calculations have been made using half the original step length without changing the results.

Comparisons of the theory with the experimental results have been given in figs 10.7 to 10.10. A good correspondence is shown in the interval $0.28 < \bar{x} < 0.47$. The differences between theory and experiment in the interval $0.15 < \bar{x} < 0.25$ may be due to different reasons. In the first place it is possible that the momentum method overestimates the effects of an oscillation in $\frac{d\bar{U}}{d\bar{x}}$ since - for cases without suction - it is essentially a one-parameter method. In the second place it is very difficult to obtain accurate values for $\frac{d\bar{U}}{d\bar{x}}$ in this region; the values given in table 10.4 and fig. 10.4 for $0.15 < \bar{x} < 0.25$ may be appreciably in error.

Between $\bar{x} = 0.46$ and 0.58 the momentum method produces values for $\bar{\delta}^*$ and H which are too high while the wall shear stress is too low. From $\bar{x} = 0.58$ to 0.635 the values for $\bar{\delta}^*$ and H are predicted too low and the wall shear stress is overestimated. Consequently the theory does not show separation. However, if the calculation is extended downstream of $\bar{x} = 0.635$ suddenly separation is obtained; this can easily be seen

as follows.

In the momentum method separation occurs at $\Lambda_1 = \bar{\theta}^2 \frac{d\bar{U}}{d\bar{x}} = -0.0871$ for the no-suction case (see table 5.3). Directly upstream of $\bar{x} = 0.635$ the calculation gives $\bar{\theta} = 0.45$ and $\Lambda_1 = -0.0525$ with $\frac{d\bar{U}}{d\bar{x}} = -0.26$. Since in the theory $\bar{\theta}$ is assumed to be continuous, even when discontinuities in the boundary conditions occur, $\bar{\theta} = 0.45$ also directly downstream of $\bar{x} = 0.635$. At this position table 10.4 indicates that $\frac{d\bar{U}}{d\bar{x}} = -0.7255$ and hence $\Lambda_1 = -0.147$; which is already far beyond the separation value of -0.0871.

It is interesting to investigate whether a small change to $\bar{U}(\bar{x})$ may be made upstream of $\bar{x} = 0.635$ which remains within experimental error and for which the momentum method predicts separation at $\bar{x} = 0.635$.

If only a very local modification is made it is easy to indicate a function $\bar{U}(\bar{x})$ which produces the desired result; this may be seen as follows.

First it is noted that due to a small change in $\bar{U}(\bar{x})$ the value of $\bar{\theta}$ at $\bar{x} = 0.635$ will not change in first approximation while $\frac{d\bar{U}}{d\bar{x}}$ and hence $\Lambda_1 = \bar{\theta}^2 \frac{d\bar{U}}{d\bar{x}}$ may change considerably. Therefore it may be assumed that $\bar{\theta}$ at $\bar{x} = 0.635$ keeps the value 0.45 so that to obtain separation at this position $\frac{d\bar{U}}{d\bar{x}}$ should assume such a value that $\Lambda_1 = \bar{\theta}^2 \frac{d\bar{U}}{d\bar{x}} = -0.0871$. This leads to $\frac{d\bar{U}}{d\bar{x}} = -0.43$. Since for the pressure distribution given in table 10.4 and fig. 10.4 the derivative $\frac{d\bar{U}}{d\bar{x}}$ changes discontinuously from -0.26 to -0.7255 at $\bar{x} = 0.635$ it is not difficult to imagine a function $\bar{U}(\bar{x})$ which produces the desired result. It is sufficient to round off the kink in $\bar{U}(\bar{x})$ at $\bar{x} = 0.635$ (see fig. 10.13). Such a modification is certainly within experimental error.

Since a local modification of $\bar{U}(\bar{x})$ does not improve the agreement between theory and experiment further upstream it is interesting to solve the more general problem of finding the function $\bar{U}(\bar{x})$ for which the momentum method reproduces the experimentally determined wall shear stress throughout a certain interval. Such a function will be indicated in the remainder of the present section.

Fig. 10.13 shows the values of $\ell = \frac{\tau_o \theta}{\mu U}$ which have been determined from the experimental results. In what follows the function $\bar{U}(\bar{x})$ will be derived for which the momentum method exactly reproduces these experimental values. Since in the momentum method for the no-suction case there is only one free parameter (see table 5.3) the known function $\ell(\bar{x})$ directly determines Λ_1 and M as function of $\bar{x}$. Then the definition of Λ_1 and the momentum equation (5.18) lead to the following differential equations for $\bar{\theta}$ and $\bar{U}$

$$\frac{d\bar{U}}{d\bar{x}} = \frac{\Lambda_1(\bar{x})}{\bar{\theta}^2} \tag{10.8}$$

$$\frac{d\bar{\theta}^2}{d\bar{x}} = \frac{M(\bar{x})}{\bar{U}(\bar{x})} \tag{10.9}$$

These equations have been solved with initial values for $\bar{U}$ and $\bar{\theta}$ at $\bar{x} = 0.46$ determined from the earlier calculation with the momentum method. The resulting function $\bar{U}(\bar{x})$ is shown in fig. 10.13. It may be seen that the difference with the original curve is certainly larger than experimental error.
However, if a similar calculation is made starting at $\bar{x} = 0.59$ the momentum method may be made to accurately predict the measured wall shear stress with a resulting change in $\bar{U}(\bar{x})$ which might be less than experimental error.

10.5.2. The multimoment method.

Near the stagnation point ($0 < \bar{x} < 0.04$) equation (10.7) supplies a good approximation of the measured pressure distribution. Hence the pressure gradient parameter λ_1 may be approximated in $0 \leqslant \bar{x} \leqslant 0.04$ by

$$\lambda_1 = 1 - 201.83\ \bar{x}^2 + 20003\ \bar{x}^4 + 4055600\ \bar{x}^6 + 207380000\ \bar{x}^8 + \ldots. \tag{10.10}$$

Using (10.10) the series method has been used to calculate the boundary layer for $0 \leqslant \bar{x} \leqslant 0.03$; the step by step method was employed for $\bar{x} \geqslant 0.03$. To be able to perform the calculations with variable step length the values of λ_1 from table 10.4 were approximated by analytic

expressions of the form (8.49). The coefficients e_n are collected in table 10.5.

Results for N = 5,6 and 7 are included in figs 10.7 - 10.12; in general a good agreement between theory and experiment is shown. It follows that the multimoment method is slightly superior to the momentum method. For instance it may be noted that a better prediction of the wall shear stress is obtained for $0.48 < \bar{x} < 0.58$. However, the deviation from the experimental values downstream of $\bar{x} = 0.58$ is very similar to the behaviour shown by the momentum method. Again no separation is indicated upstream of $\bar{x} = 0.635$. If however the calculation is extended beyond $\bar{x} = 0.635$ suddenly separation occurs.

Again small changes in $\bar{U}(\bar{x})$ upstream of $\bar{x} = 0.635$ are sufficient to let the theory "predict" the wall shear stress with good accuracy in the interval shortly upstream of $\bar{x} = 0.635$.

10.6. Concluding remarks on the experiments without suction.

From the comparisons between theory and experiment for the boundary layer without suction the following conclusions may be drawn.

1. Both the momentum method and the multimoment provide results which are in good agreement with the experiments except close to separation. The multimoment method is slightly superior to the momentum method.
2. Both methods fail to predict separation if the pressure distribution from fig. 10.4 and table 10.4 is used. Both theories may be forced to approach separation with the right shear stress distribution by changing $\bar{U}(\bar{x})$ with a small amount. Although this change might be within experimental error no firm conclusion has been reached on this point.
3. To provide a definite answer to the question whether boundary layer theory is valid near separation the experiments should be performed with greater accuracy than has been achieved in the present investigation.

Table 10.1: Coordinates of impervious airfoil section.

$x_{p/c}$ %	$y_{p/c}$ %	$x_{p/c}$ %	$y_{p/c}$ %	$x_{p/c}$ %	$y_{p/c}$ %
0	0	20	12.25	70	10.32
0.5	2.58	25	12.98	75	9.10
1	3.69	30	13.48	80	7.70
2	5.03	35	13.82	85	6.09
3	6.07	40	13.92	90	4.32
4	6.89	45	13.80	95	2.41
5	7.55	50	13.50	100	0.26
7.5	8.90	55	13.00		
10	9.83	60	12.30		
15	11.21	65	11.41		

Table 10.2: Position of pressure orifices in the impervious model.

no	Chord I			Chord II
	$x_{p/c}$ %	$y_{p/c}$ %	s/c %	s/c %
1	1.84	-4.92	-5.42	-5.41
2	0.46	-2.53	-2.68	-2.70
3	0.25	-2.00	-2.20	--
4	0.16	-1.50	-1.58	--
5	0.09	-1.03	-1.09	-1.08
6	0.03	-0.50	-0.48	-0.49
7	0	0	0	0
8	0.03	+0.50	+0.53	+0.49
9	0.10	1.10	1.11	--
10	0.26	1.68	1.61	--
11	0.40	2.18	2.21	--
12	0.53	2.59	2.72	2.72
13	0.74	3.08	3.24	--
14	1.31	4.03	4.32	--
15	2.75	5.78	6.52	6.49
16	4.75	7.44	9.19	--
17	6.20	8.29	10.88	10.83
18	10.67	10.06	15.64	--
19	16.35	11.55	21.67	21.63
20	21.18	12.45	26.52	--
21	26.95	13.20	32.41	32.44

no	Chord I			Chord II
	$x_{p/c}$ %	$y_{p/c}$ %	s/c %	s/c %
22	32.30	13.65	37.85	37.87
23	35.55	13.82	40.97	--
24	43.18	13.90	48.61	--
25	48.58	13.63	54.04	54.02
26	53.91	13.18	59.42	--
27	59.25	12.44	64.82	64.81
28	65.13	11.43	70.83	--
29	69.85	10.37	75.62	75.62
30	75.10	9.11	81.04	--
31	80.25	7.63	86.44	86.41
32	85.42	5.98	91.79	--
33	90.35	4.23	97.20	97.22
34	95.41	2.25	102.63	--
35	--	--	49.51	--
36	--	--	53.47	--
37	--	--	54.97	--
38	--	--	58.77	--
39	--	--	61.27	--
40	--	--	65.36	--
41	--	--	67.35	--
tr.edge	100	0.26	107.90	107.75

Table 10.3. Results of pressure distribution measurements on the impervious model

$\bar{U}$ from orifices			$\bar{U}$ from surface tubes in chord I (in the same order as measured)			
no	chord I	chord II	$\bar{x}$	$\bar{U}$	$\bar{x}$	$\bar{U}$
1	-0.9713	-0.9665	0.780	1.2101	0.449	1.3628
2	-0.5670	-0.5659	0.757	1.2222	427	1.3607
3	-0.4718	-	0.734	1.2367	408	1.3576
4	-0.3454	-	0.729	1.2407	387	1.3543
5	-0.2411	-0.2416	725	1.2456	368	1.3524
6	-0.1110	-0.1196	718	1.2534	328	1.3490
7	±0.0575	±0.0648	709	1.2806	288	1.3447
8	±0.1196	±0.1273	699	1.2963	266	1.3417
9	+0.2416	-	690	1.2979	248	1.3405
10	+0.3415	-	679	1.3001	328	1.3487
11	0.4631	-	669	1.3027	229	1.3379
12	0.5513	+0.5582	659	1.3063	209	1.3311
13	0.6424	-	649	1.3091	189	1.3258
14	0.8078	-	644	1.3118	189	1.3232
15	1.0693	+1.0742	6395	1.3135	168	1.3170
16	1.2340	-	6335	1.3162	149	1.3146
17	1.2866	1.2803	609	1.3233	149	1.3154
18	1.3224	-	618	1.3204	139	1.3163
19	1.3432	-	578	1.3324	128	1.3154
20	1.3467	-	538	1.3464	128	1.3102
21	1.3576	1.3585	519	1.3540	118	1.3039
22	1.3631	1.3678	4985	1.3629	107	1.2778
23	1.3649	-	487	1.3649	097	1.2504
24	1.3735	-	479	1.3656	063	1.0490
25	1.3553	1.3602	468	1.3658	199	1.3276
26	1.3350	-	449	1.3635	178	1.3197
27	1.3187	1.3167			158	1.3158
28	1.2881	-				
29	1.2221	1.2276				
30	1.1855	-				
31	1.1371	1.1413				
32	1.0751	-				
33	0.9950	0.9970				
34	0.8983	-				
35	1.3722	-				
36	1.3579	-				
37	1.3512	-				
38	1.3392	-				
39	1.3318	-				
40	1.3156	-				
41	1.3085	-				

Table 10.4: Pressure distribution used in the boundary layer calculations for the impervious model.

$\bar{x}$	$\bar{U}$	$\frac{d\bar{U}}{d\bar{x}}$	$\lambda_1 = \frac{\bar{x}}{\bar{U}} \frac{d\bar{U}}{d\bar{x}}$	$\bar{x}$	$\bar{U}$	$\frac{d\bar{U}}{d\bar{x}}$	$\lambda_1 = \frac{\bar{x}}{\bar{U}} \frac{d\bar{U}}{d\bar{x}}$
0.04	0.7610	14.180	0.7453	0.35	1.35825	0,0995	0.0256
0.05	0.9070	11.770	0.6488	0.36	1.35925	0.1015	0.0269
0.06	1.0194	9.565	0.5630	0.37	1.36025	0.1055	0.0287
0.07	1.1046	7.541	0.4779	0.38	1.36135	0.1115	0.0311
0.08	1.1720	5.988	0.4087	0.39	1.36255	0.1200	0.0343
0.09	1.2251	4.643	0.3411	0.40	1.36375	0.1305	0.0383
0.10	1.2653	3.4224	0.2705	0.41	1.36510	0.1430	0.0429
0.11	1.2939	2.3027	0.1958	0.42	1.36655	0.1540	0.0473
0.12	1.3120	1.4777	0.1356	0.43	1.36815	0.1610	0.0506
0.13	1.32235	0.6082	0.0598	0.44	1.36975	0.1640	0.0527
0.14	1.32465	-0.1057	-0.0112	0.45	1.37135	0.1630	0.0535
0.15	1.32270	-0.1421	-0.0161	0.46	1.37285	0.1500	0.0503
0.16	1.32235	+0.0623	+0.0075	0.47	1.37395	0.0700	0.0239
0.17	1.3239	0.2394	0.0308	0.48	1.37425	-0.0192	-0.0067
0.18	1.3269	0.3565	0.0484	0.49	1.37325	-0.1806	-0.0644
0.19	1.3308	0.4133	0.0590	0.50	1.37075	-0.3152	-0.1150
0.20	1.33495	0.4089	0.0613	0.51	1.36730	-0.3709	-0.1383
0.21	1.3388	0.3476	0.0545	0.52	1.36340	-0.4050	-0.1556
0.22	1.3418	0.2587	0.0424	0.53	1.35930	-0.4111	-0.1603
0.23	1.3441	0.2030	0.0347	0.54	1.35520	-0.4059	-0.1617
0.24	1.3459	0.1630	0.0291	0.55	1.35125	-0.3799	-0.1546
0.25	1.3474	0.1405	0.0261	0.56	1.34765	-0.3452	-0.1434
0.26	1.34875	0.1275	0.0246	0.57	1.34430	-0.3240	-0.1374
0.27	1.34995	0.1170	0.0234	0.58	1.34115	-0.3048	-0.1318
0.28	1.35115	0.1090	0.0226	0.59	1.33819	-0.2900	-0.1279
0.29	1.35225	0.1041	0.0223	0.60	1.33534	-0.2793	-0.1254
0.30	1.35325	0.1005	0.0223	0.61	1.33260	-0.2709	-0.124
0.31	1.35425	0.0990	0.0227	0.62	1.32991	-0.2646	-0.1234
0.32	1.35525	0.0980	0.0231	0.63	1.32730	-0.2608	-0.1238
0.33	1.35625	0.0980	0.0238	0.635	1.32600	-0.2600	-0.1245
0.34	1.35725	0.0980	0.0245	0.635	1.32600	-0.7255	-0.34743

Table 10.5: Coefficients in equation (8.49): $\lambda_1 = \sum_{n=0}^{6} e_n \bar{x}^n$ for the impervious model (0.543 + 2 denotes $0.543 \times 10^{+2}$)

n	e_n for				
	$0.04 \leq \bar{x} < 0.14$	$0.14 \leq \bar{x} < 0.24$	$0.24 \leq \bar{x} < 0.456$	$0.456 \leq \bar{x} < 0.54$	$0.54 \leq \bar{x} < 0.635$
0	+0.4777781+0	+0.468318718+2	+0.283142524+2	-0.441984929+3	+0.62238306+2
1	+0.4725992+2	-0.108946502+4	-0.521724645+3	+0.275812516+4	-0.343194183+2
2	-0.1947334+4	+0.903993722+4	+0.396976398+4	-0.492329408+4	+0.62179067+3
3	+0.3319732+5	-0.267304210+5	-0.159384857+5	-0.458252779+3	-0.46537777+3
4	-0.2968925+6	-0.319871038+5	+0.355911081+5	+0.667306127+4	+0.60355487+3
5	+0.1349858+7	+0.332606988+6	-0.418994924+5	+0.604744491+3	-0.12214455+4
6	-0.2467063+7	-0.498304819+6	+0.203209638+5	-0.544276543+4	+0.79281632+3

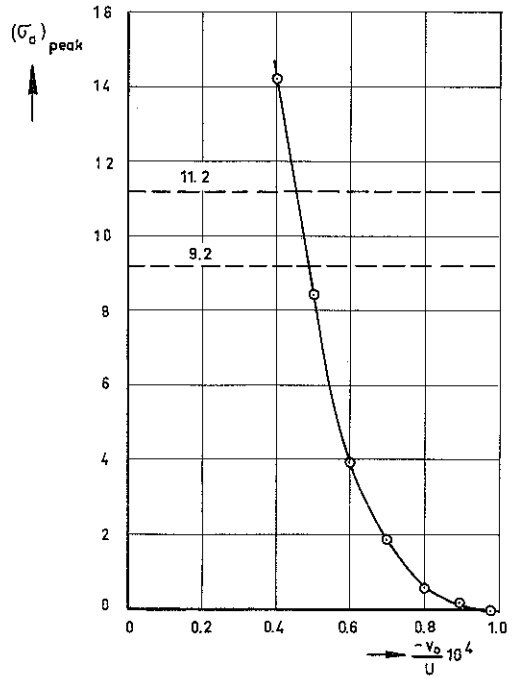

FIG.9.24 : CROSS PLOT FROM FIG.9.23; PEAK AMPLIFICATION FACTOR FOR THE FLAT PLATE WITH CONSTANT SUCTION VELOCITY.

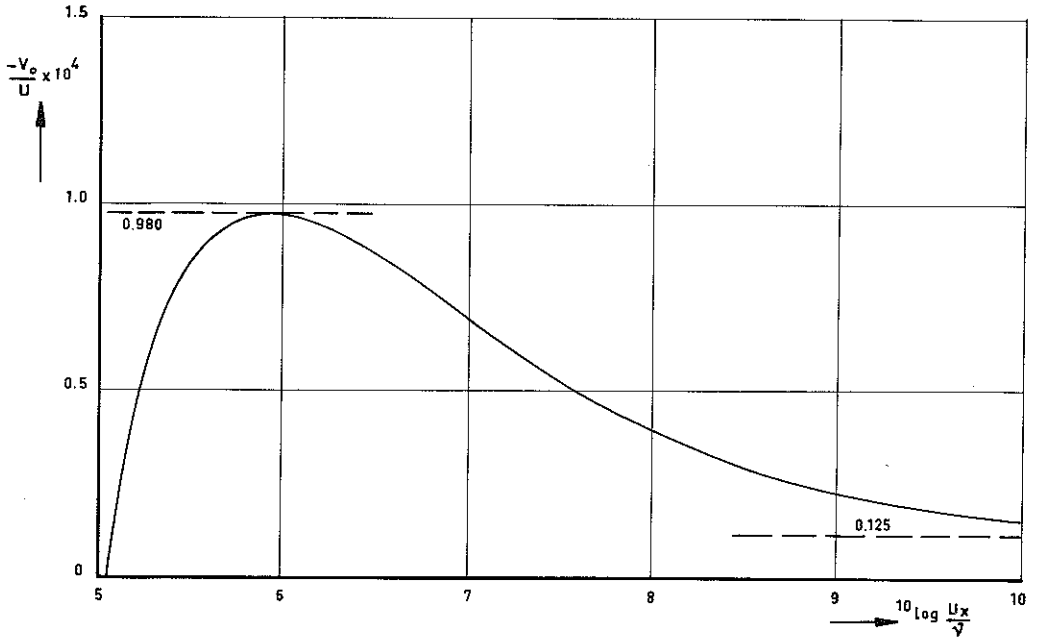

FIG.9.25 : SUCTION DISTRIBUTION REQUIRED FOR THE FLAT PLATE TO MAINTAIN A NEUTRALLY STABLE BOUNDARY LAYER DOWNSTREAM OF THE INSTABILITY POINT.

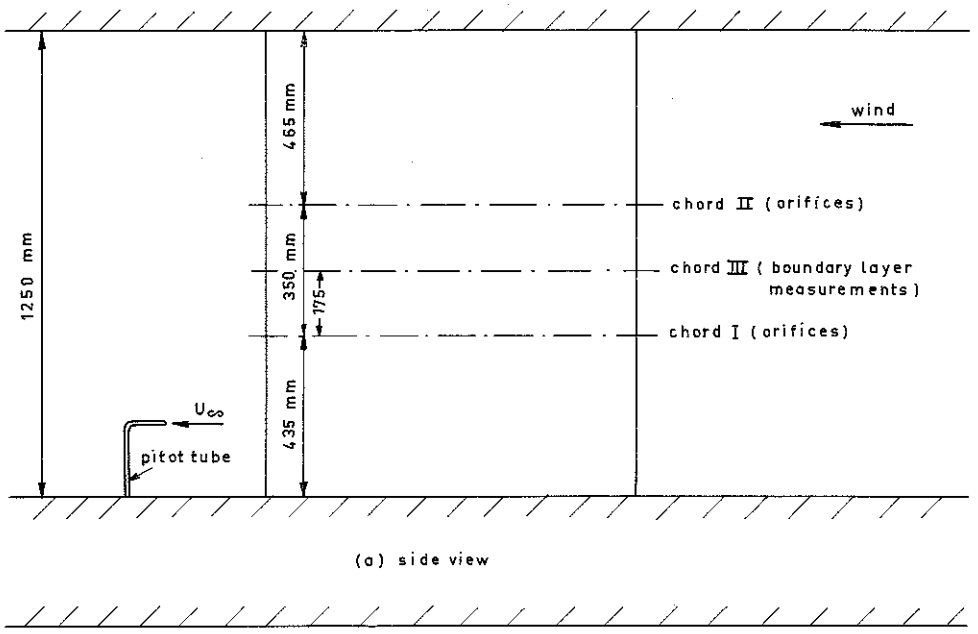

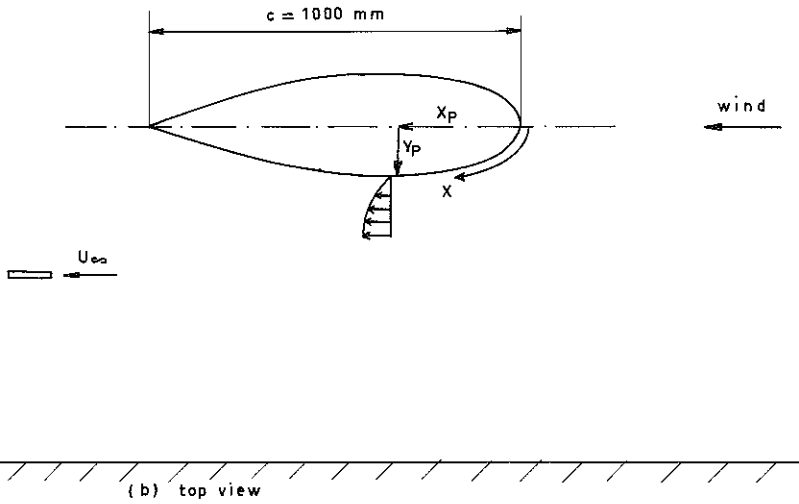

FIG. 10,1 : SET UP OF IMPERVIOUS AIRFOIL SECTION IN WINDTUNNEL

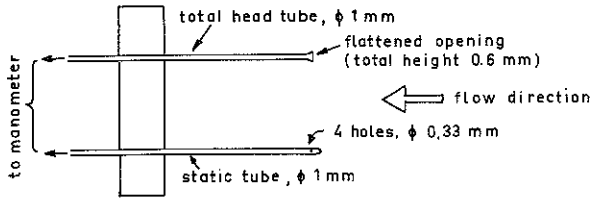

FIG. 10.2: COMBINED TOTAL HEAD-AND STATIC TUBE

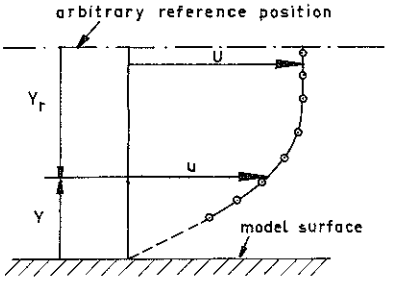

FIG. 10.3: DEFINITIONS USED IN HOT WIRE MEASUREMENTS

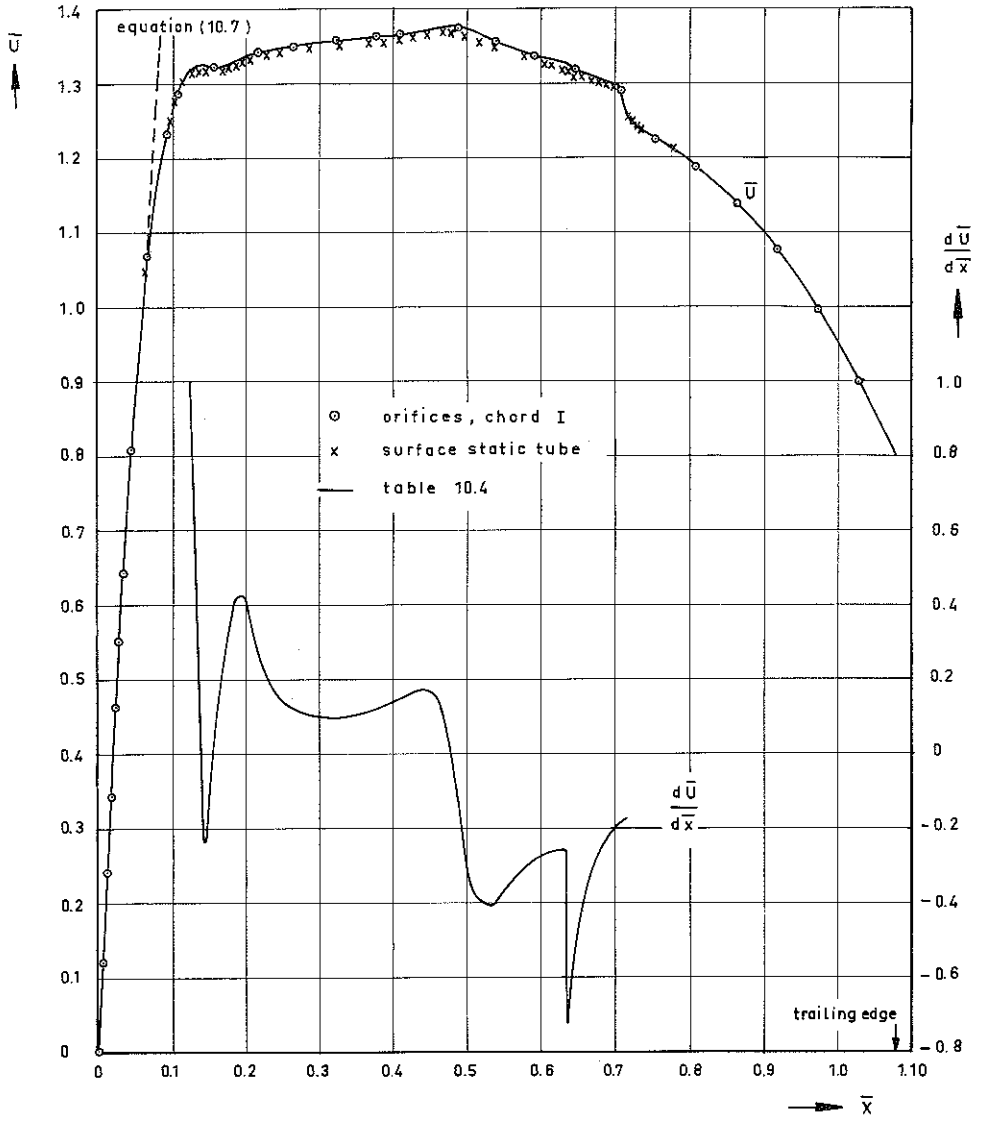

FIG. 10.4: RESULTS OF PRESSURE DISTRUBUTION MEASURUMENTS IN CHORD NUMBER I

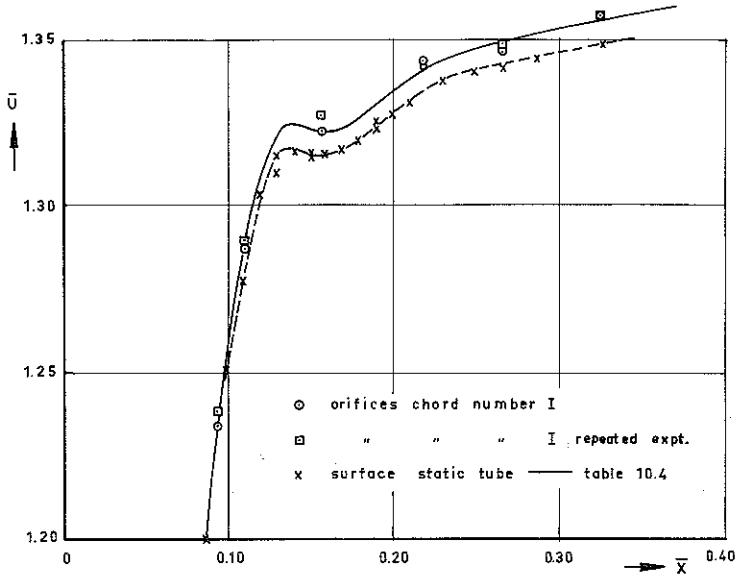

FIG.10.5: $\bar{U}$ ($\bar{X}$) NEAR LEADING EDGE.

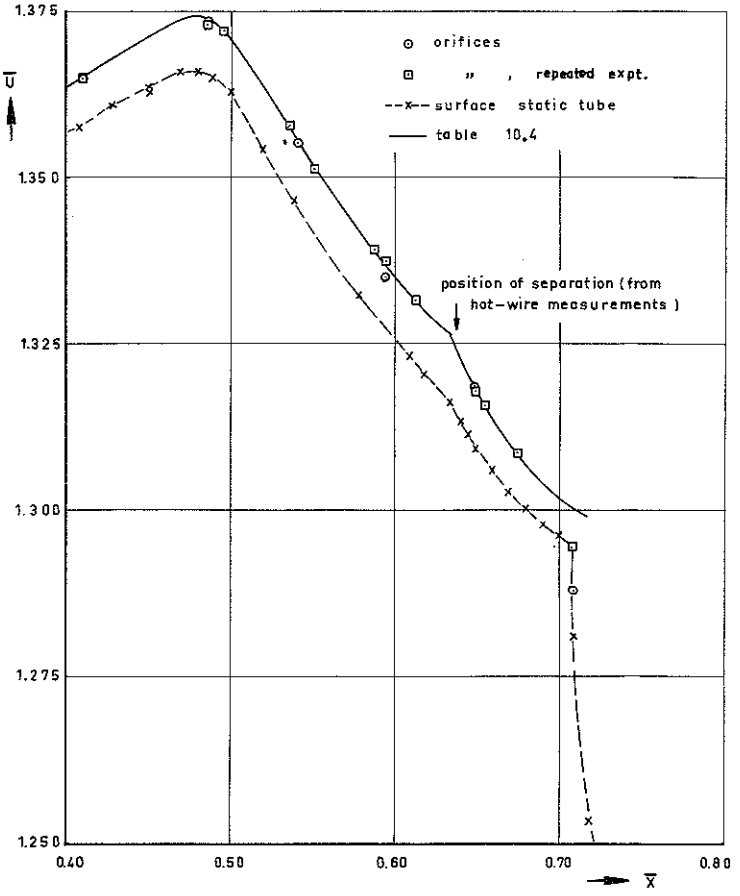

FIG.10.6: $\bar{U}$ ($\bar{X}$) IN REGION OF SEPARATION (CHORD I)

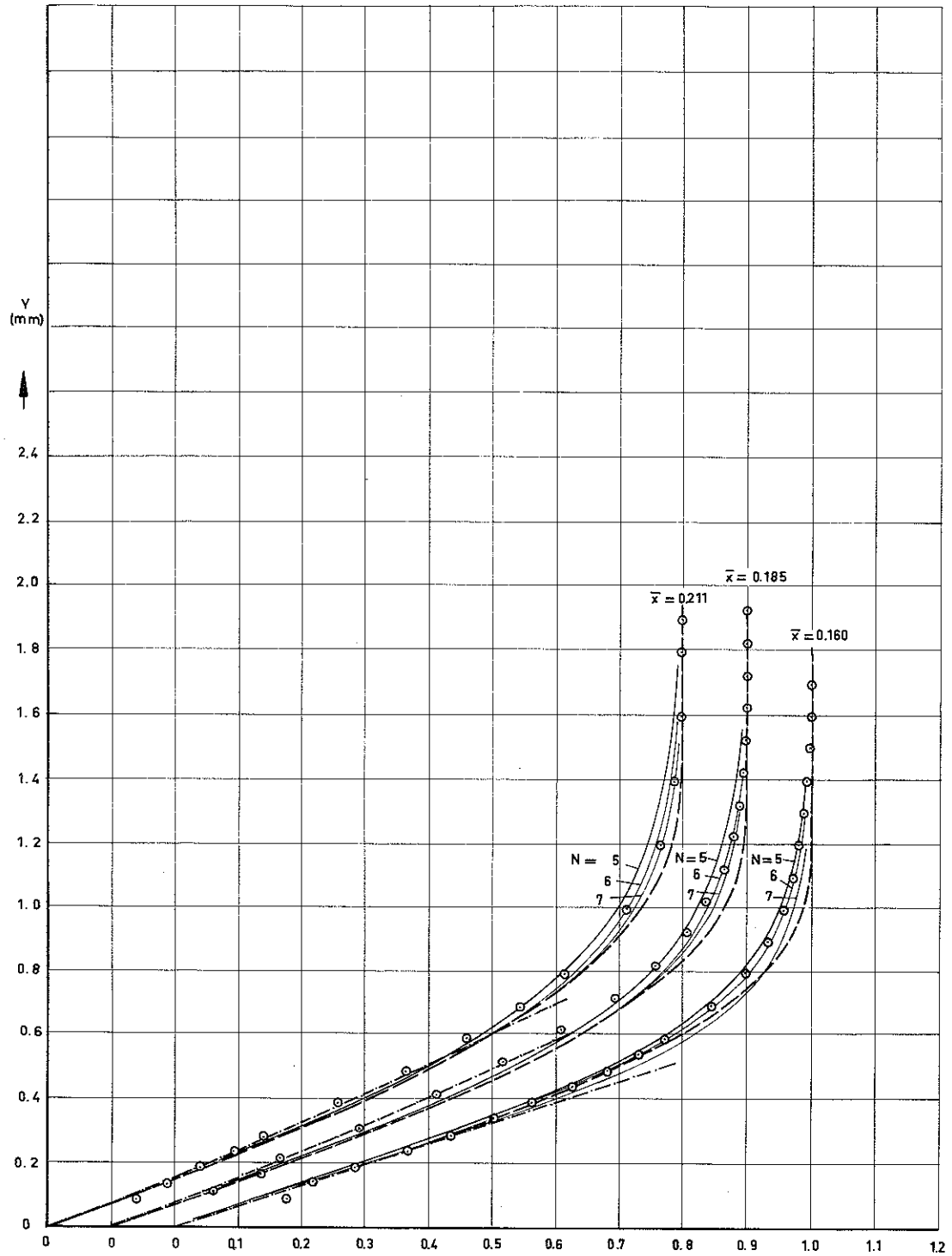

FIG.10.7 A : BOUNDARY LAYER VELOCITY PROFILES FOR THE IMPERVIOUS MODEL ; → $\bar{u}$

(+,⊙ EXPERIMENT, – – – momentum method, —— multimoment method. , —·—·— e.q. (10.4)

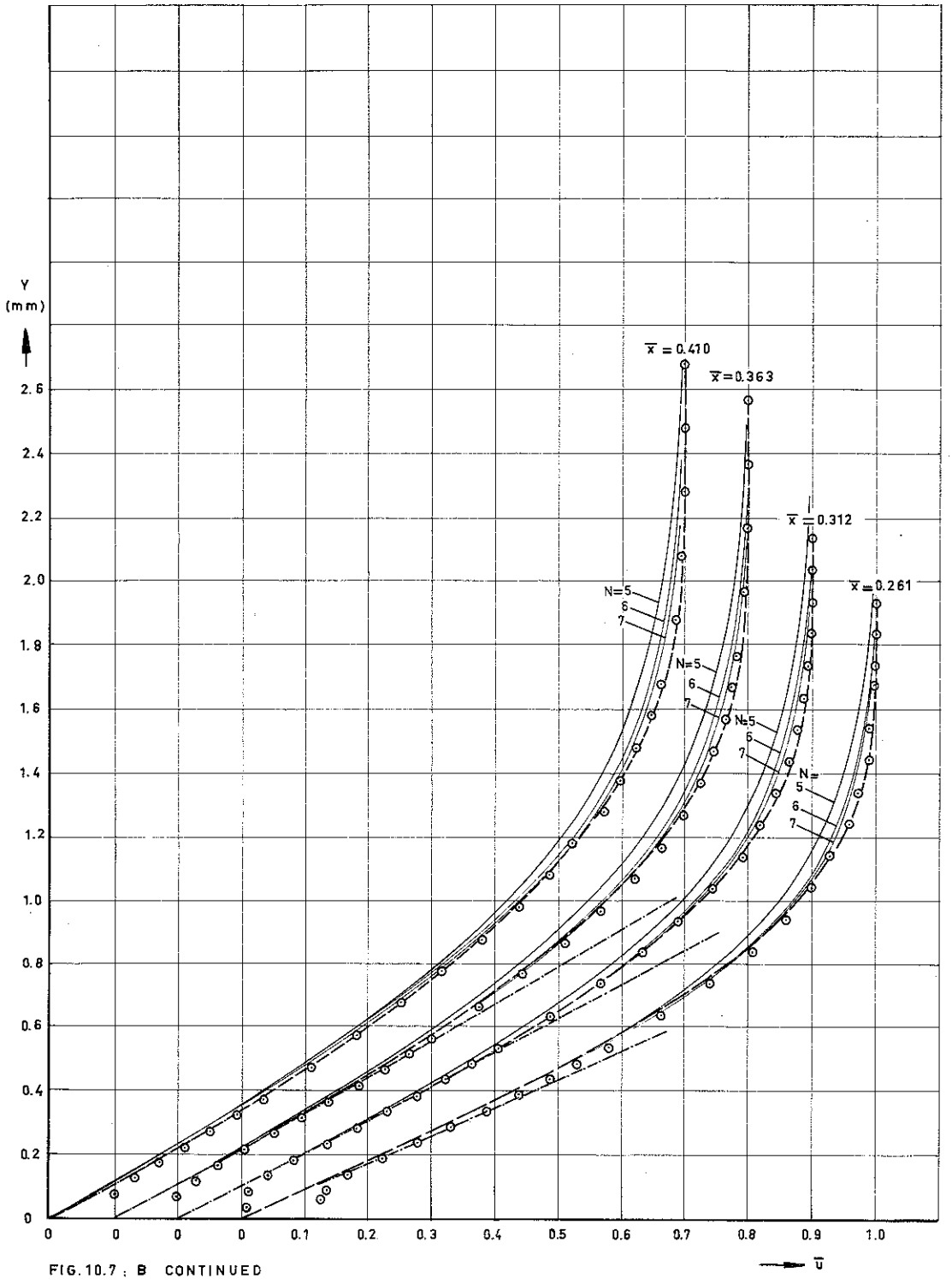

FIG. 10.7 ; B CONTINUED

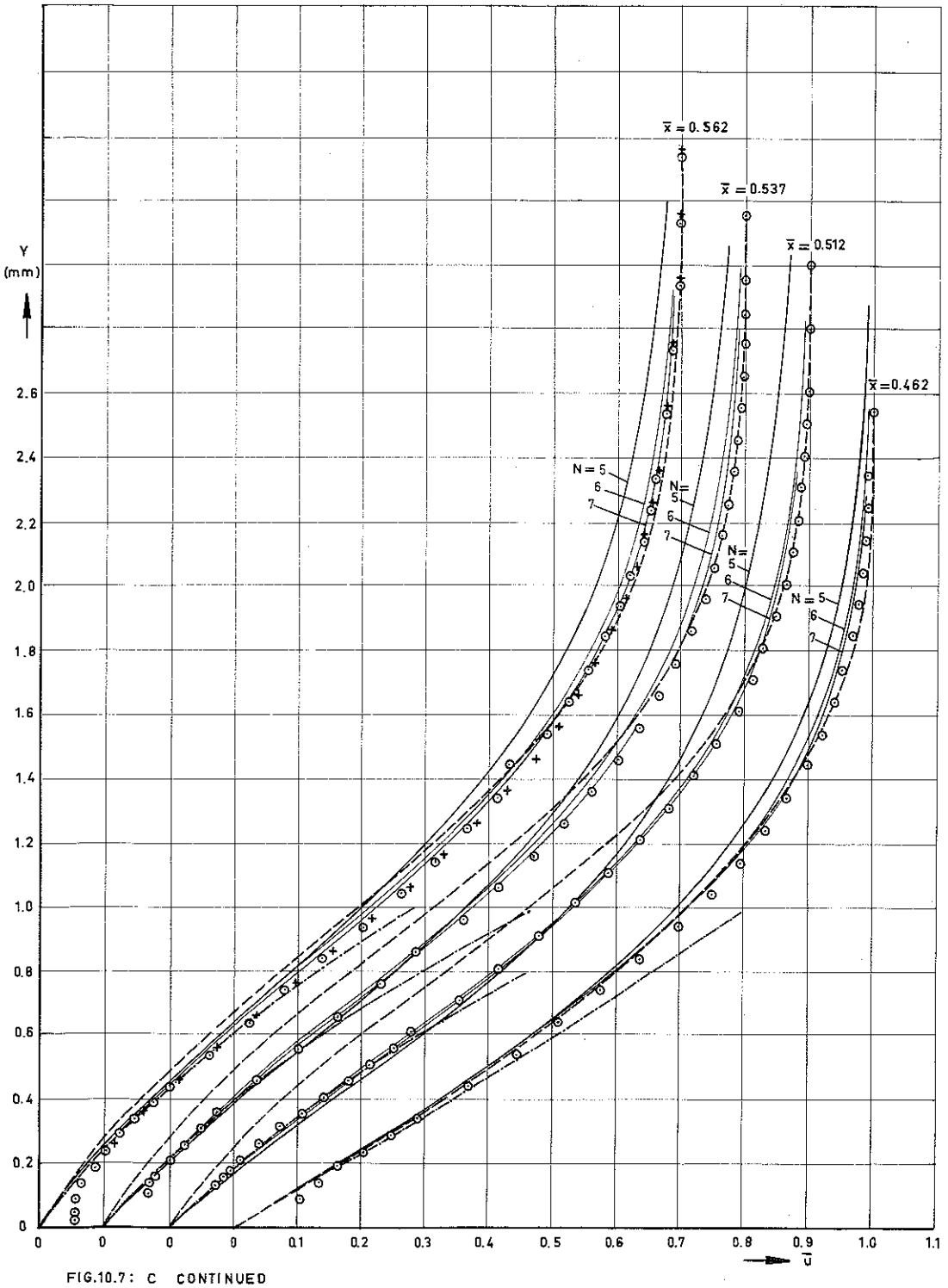

FIG.10.7: C CONTINUED

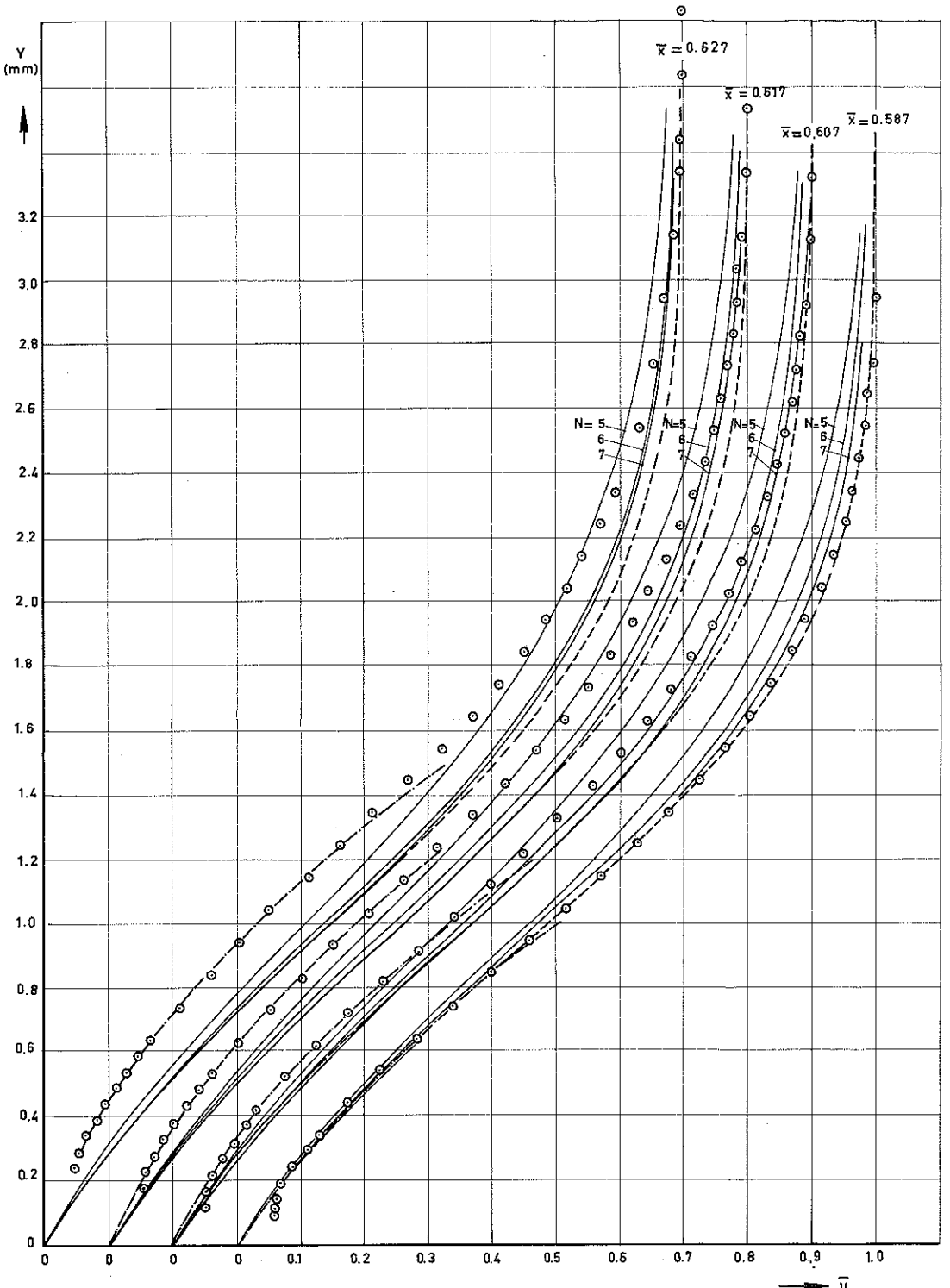

FIG. 10.7 : D CONCLUDED

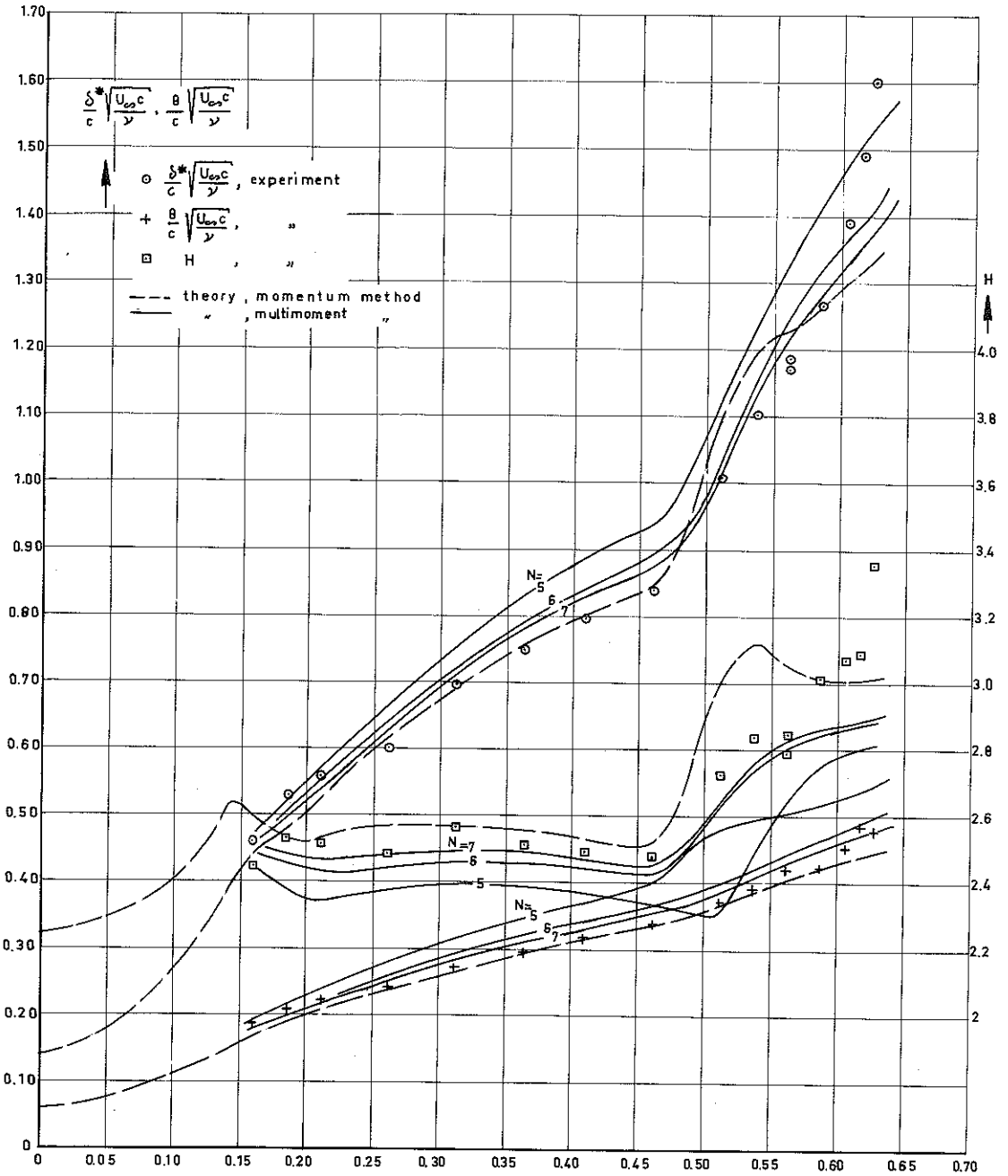

FIG. 10.8: SOME BOUNDARY LAYER PARAMETERS FOR THE IMPERVIOUS AIRFOIL.

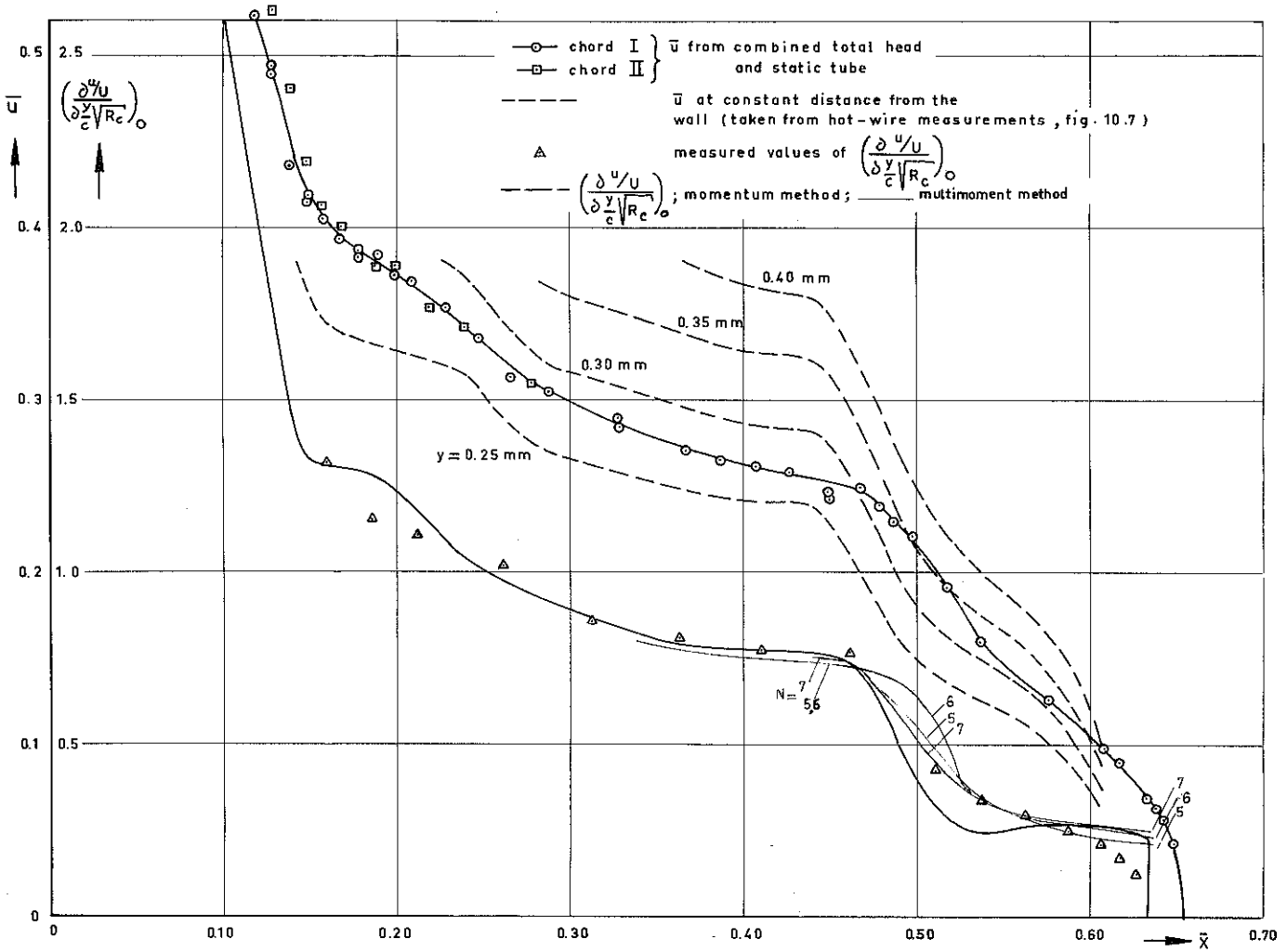

FIG. 10.9: RESULTS OF THEORY AND EXPERIMENT FOR THE WALL SHEAR STRESS; COMPARISON WITH RESULTS OBTAINED FROM THE COMBINED TOTAL HEAD-AND STATIC TUBE.

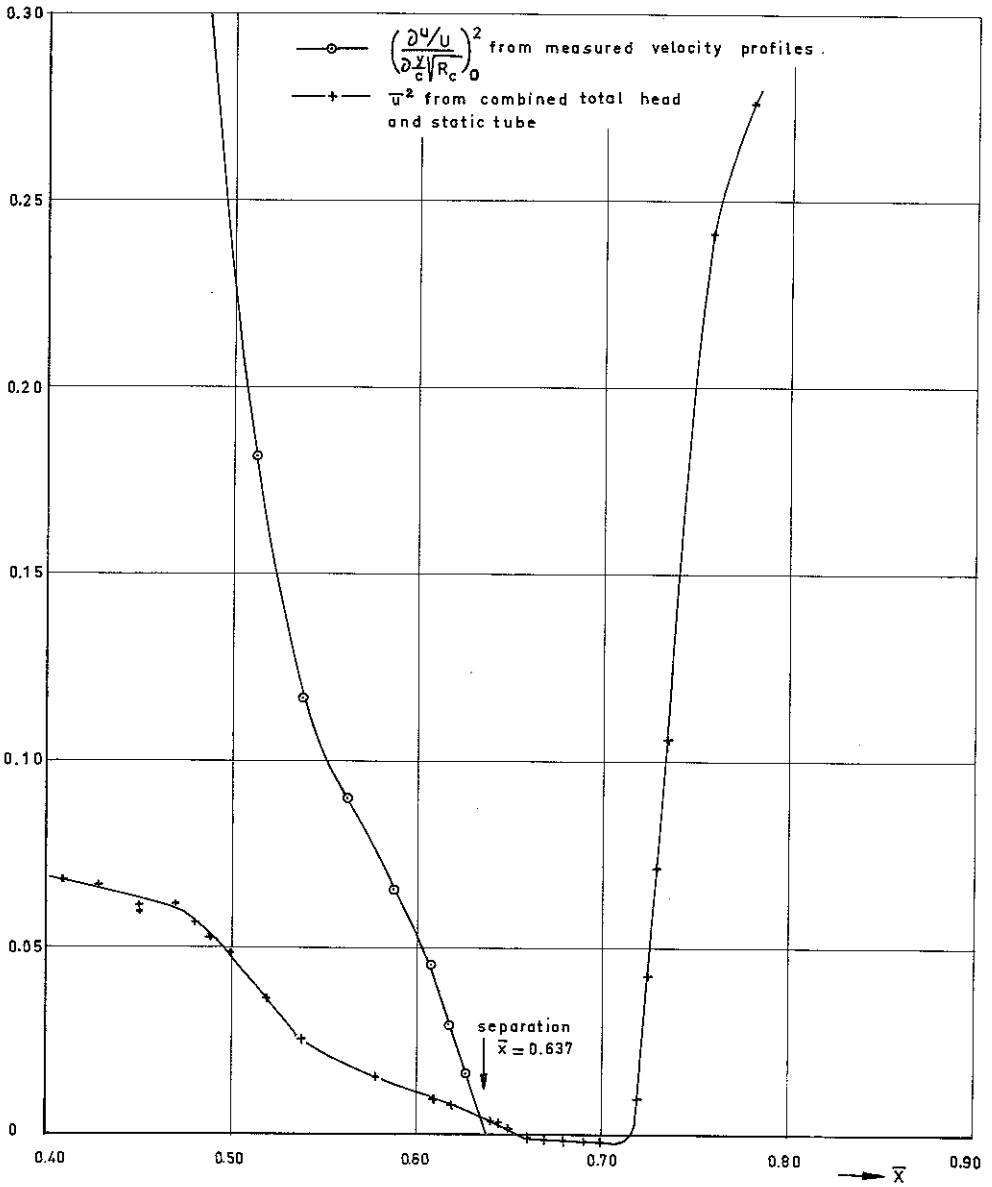

FIG.10.10 : SQUARE OF WALL SHEAR STRESS NEAR SEPARATION AND RESULTS OBTAINED FROM COMBINED TOTAL-HEAD AND STATIC TUBE.

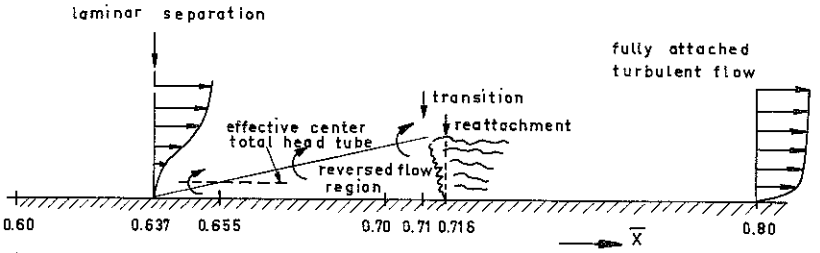

FIG.10.11: SCHEMATIC DESCRIPTION OF FLOW IN SEPARATED REGION.

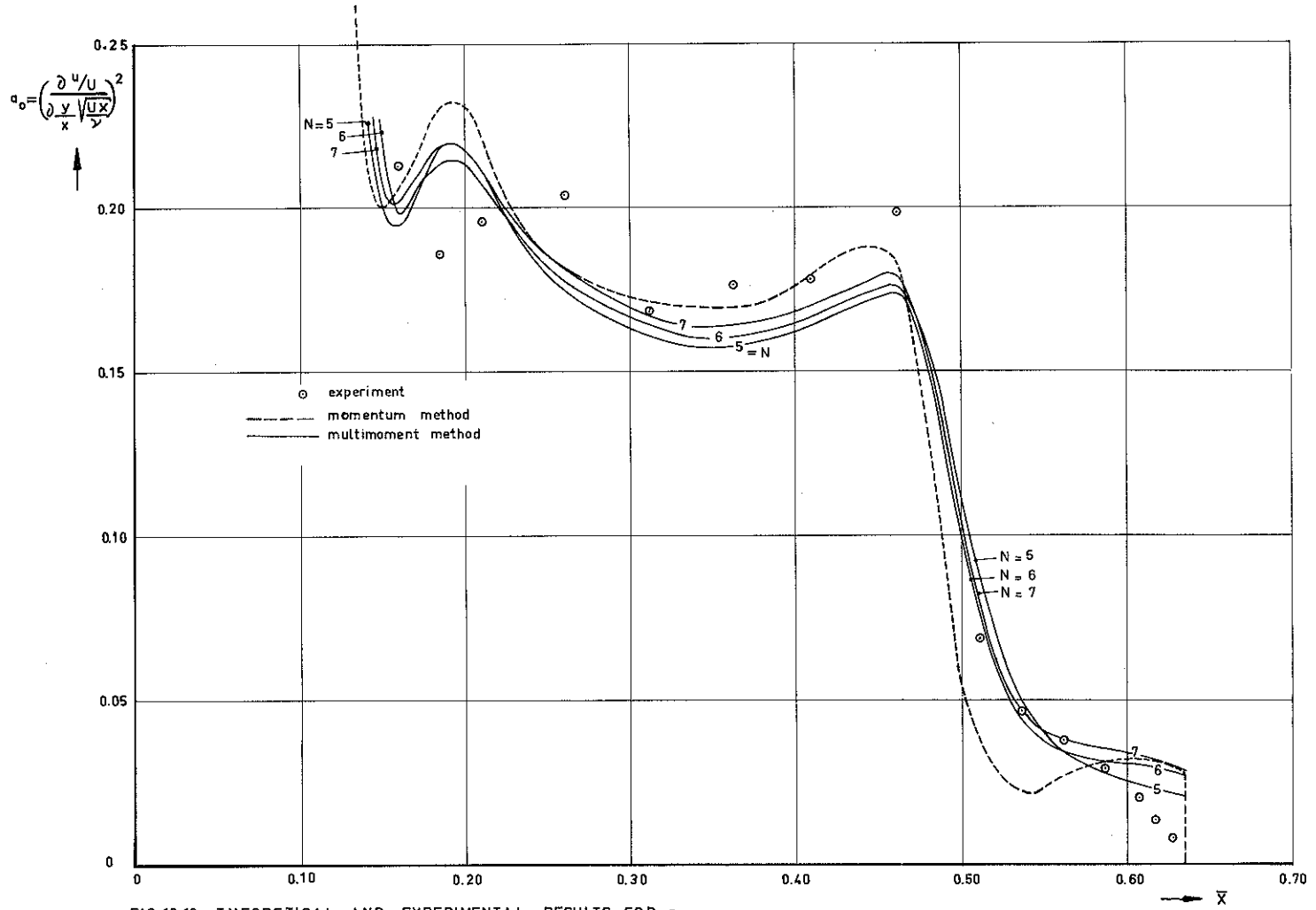

FIG.10.12: THEORETICAL AND EXPERIMENTAL RESULTS FOR a_0

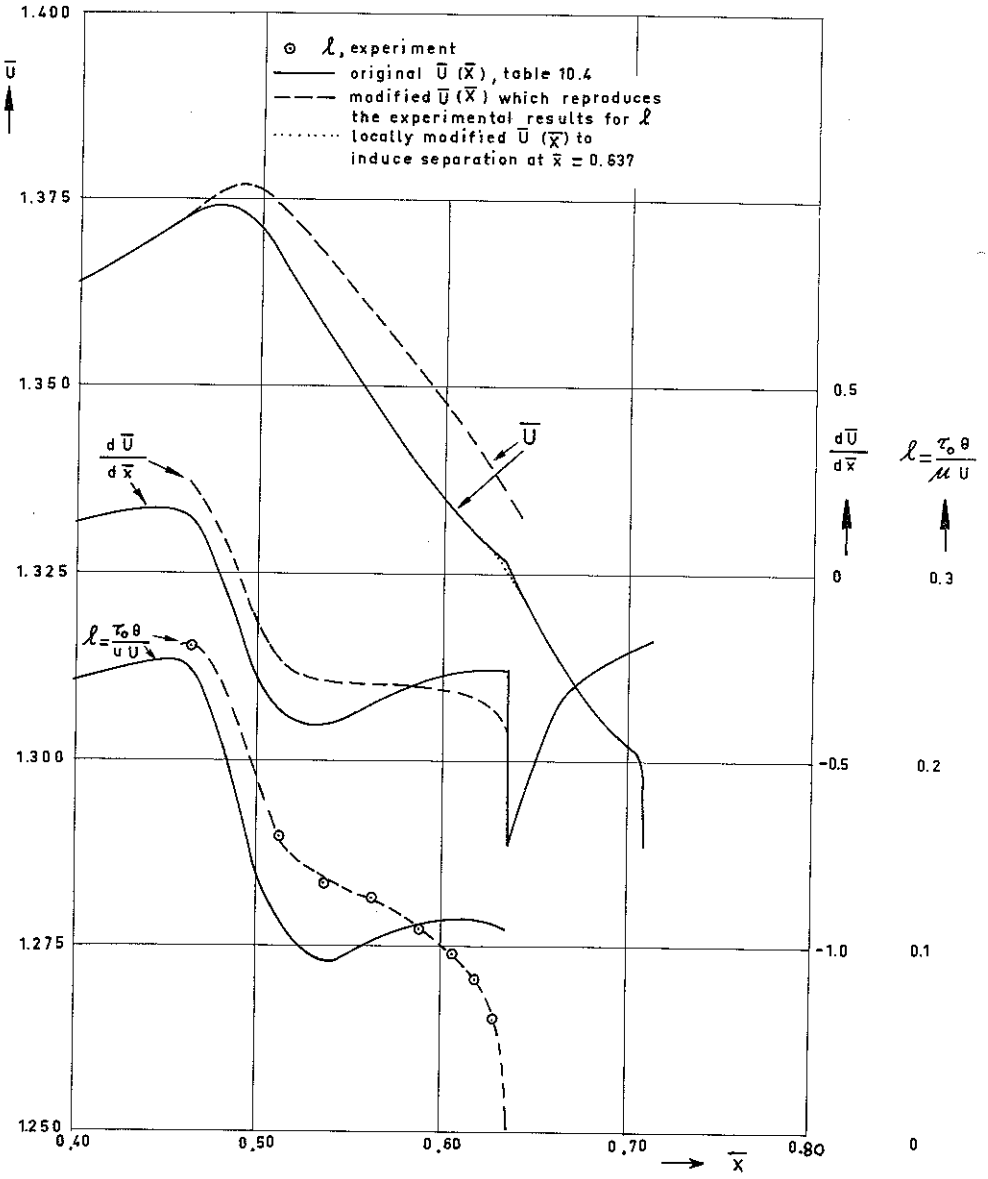

FIG. 10.13: EFFECT OF MODIFICATIONS IN $\bar{U}(\bar{x})$ ON RESULTS OF THE MOMENTUM METHOD.